



Continuation of long-term global SO₂ pollution monitoring from OMI to OMPS

Yan Zhang^{1,2}, Can Li^{1,2}, Nikolay A. Krotkov², Joanna Joiner², Vitali Fioletov³, and Chris McLinden³

¹Earth System Science Interdisciplinary Center, University of Maryland, College Park, MD 20742, USA

²NASA Goddard Space Flight Center, Greenbelt, MD 20771, USA

³Air Quality Research Division, Environment Canada, Toronto, ON, Canada

Correspondence to: Yan Zhang (yan.zhang@nasa.gov)

Received: 5 July 2016 – Discussion started: 2 November 2016

Revised: 21 March 2017 – Accepted: 23 March 2017 – Published: 20 April 2017

Abstract. Over the past 20 years, advances in satellite remote sensing of pollution-relevant species have made spaceborne observations an increasingly important part of atmospheric chemistry research and air quality management. This progress has been facilitated by advanced UV–vis spectrometers, such as the Ozone Monitoring Instrument (OMI) on board the NASA Earth Observing System (EOS) Aura satellite, and continues with new instruments, such as the Ozone Mapping and Profiler Suite (OMPS) on board the NASA–NOAA Suomi National Polar-orbiting Partnership (SNPP) satellite. In this study, we demonstrate that it is possible, using our state-of-the-art principal component analysis (PCA) retrieval technique, to continue the long-term global SO₂ pollution monitoring started by OMI with the current and future OMPS instruments that will fly on the NOAA Joint Polar Satellite System (JPSS) 1, 2, 3, and 4 satellites in addition to SNPP, with a very good consistency of retrievals from these instruments. Since OMI SO₂ data have been primarily used for (1) providing regional context on air pollution and long-range transport on a daily basis and (2) providing information on point emission sources on an annual basis after data averaging, we focused on these two aspects in our OMI–OMPS comparisons. Four years of retrievals (2012–2015) have been compared for three regions: eastern China, Mexico, and South Africa. In general, the comparisons show relatively high correlations ($r = 0.79$ – 0.96) of daily regional averaged SO₂ mass between the two instruments and near-unity regression slopes (0.76 – 0.97). The annual averaged SO₂ loading differences between OMI and OMPS are small (< 0.03 Dobson unit (DU) over South Africa and up to 0.1 DU over eastern China). We also found a

very good correlation ($r = 0.92$ – 0.97) in the spatial distribution of annual averaged SO₂ between OMI and OMPS over the three regions during 2012–2015. The emissions from ~ 400 SO₂ sources calculated with the two instruments also show a very good correlation ($r \sim 0.9$) in each year during 2012–2015. OMPS-detected SO₂ point source emissions are slightly lower than those from OMI, but OMI–OMPS differences decrease with increasing strength of source. The OMI–OMPS SO₂ mass differences on a pixel by pixel (daily) basis in each region can show substantial differences. The two instruments have a spatial correlation coefficient of 0.7 or better on $< \sim 50\%$ of the days. It is worth noting that consistent SO₂ retrievals were achieved without any explicit adjustments to OMI or OMPS radiance data and that the retrieval agreement may be further improved by introducing a more comprehensive Jacobian lookup table than is currently used.

1 Introduction

Sulfur dioxide (SO₂) is an important pollutant gas that has significant impacts on the environment and climate at global, regional, and local scales. It oxidizes to form sulfate aerosols that reduce visibility, affect cloud formation, and lead to acid rain and deposition. Anthropogenic sources of SO₂, consisting primarily of fossil fuel burning (Fioletov et al., 2015; Li et al., 2010a, b), metal smelting (Carn et al., 2007), and oil and gas refining (McLinden et al., 2014), contribute roughly 70 % of global SO₂ emissions (Smith et al., 2011). The remainder of SO₂ emissions come from natural sources, e.g.,

volcanic eruptions and degassing and sea spray (Faloona et al., 2010).

Space-based SO₂ retrievals were first demonstrated for the El Chichón volcanic eruption using the Total Ozone Mapping Spectrometer (TOMS) (Krueger, 1983). Since then, satellite retrievals of global SO₂ pollution have undergone substantial improvements. Satellite remote sensing using spectral fitting techniques in the ultraviolet (UV) has been employed for global retrievals of SO₂ total columns (Eisinger and Burrows, 1998; Fioletov et al., 2013; Krotkov et al., 2016; Li et al., 2013; Theys et al., 2015). Measurements of anthropogenic SO₂ have been demonstrated using several hyperspectral UV spectrometers such as the Global Ozone Monitoring Experiment (GOME) (e.g., Eisinger and Burrows, 1998), GOME-2 (Nowlan et al., 2011), SCanning Imaging Absorption SpectroMeter for Atmospheric CHartography (SCIAMACHY) (Lee et al., 2009), Ozone Monitoring Instrument (OMI) (Krotkov et al., 2006, 2008, 2016; Li et al., 2010a, b; Fioletov et al., 2015; McLinden et al., 2014, 2016a), and the nadir mapper of the Ozone Mapping and Profiler Suite (OMPS) (Yang et al., 2013). However, it is challenging to build consistent, multi-satellite datasets necessary for long-term monitoring and trend studies, as different characteristics between satellite instruments must be accounted for; relatively small inconsistencies in satellite radiance measurements and calibration may introduce large retrieval biases. Previous studies also suggested that the spatial resolution of a satellite instrument is the main limiting factor in detection of SO₂ emissions from point sources (Fioletov et al., 2013, 2015). This is because the coarse spatial resolution will dilute the derived SO₂ columns or masses for point sources as compared with fine spatial resolution. This causes additional measurement differences in SO₂ loading from different instruments. Stitching together satellite SO₂ retrievals from different instruments and processed with various algorithms therefore usually requires empirical SO₂ bias corrections (Fioletov et al., 2013).

Recently, a principal component analysis (PCA) SO₂ algorithm was developed and applied to OMI (Li et al., 2013, 2017). This approach greatly reduces the noise and bias compared with the previous band residual difference (BRD) OMI SO₂ algorithm (Krotkov et al., 2006), allows smaller sources to be detected from space (Fioletov et al., 2015, 2016; McLinden et al., 2016b), and enables trends to be studied for more regions. One of the strengths of the PCA technique is that it does not require instrument-specific, explicit corrections to satellite-measured radiance data. This makes it relatively straightforward to adapt to other instruments and reduces the chance of introducing retrieval biases between different instruments. In this paper we apply the PCA technique to OMPS measurements (2012–2015) to examine the feasibility of continuing the OMI anthropogenic SO₂ dataset with OMPS.

2 OMI and OMPS SO₂ data

2.1 OMI operational PCA planetary boundary layer (PBL) SO₂

OMI is a nadir-viewing UV–visible spectrometer (Levelt et al., 2006a) on board NASA's Aura satellite launched in 2004 (Schoeberl et al., 2006). It measures sunlight backscattered from the Earth and solar irradiance covering the wavelength range from 270 to 500 nm at approximately 0.5–0.6 nm spectral resolutions. The nominal pixel size of OMI is ~ 13 km by 24 km at nadir and ~ 28 km by 150 km at the swath edges. The swath is ~ 2600 km wide and contains 60 cross-track binned field of views (FOVs or “rows” on a two-dimensional CCD detector). The current local Equator crossing time is about 13:38 local time (LT). OMI measurement of SO₂ is one of the key objectives of the OMI mission (Levelt et al., 2006b).

This study focuses on anthropogenic SO₂ that is mainly distributed within the PBL near source regions. Therefore we use the OMI operational PCA PBL SO₂ product (OMSO2 v1.2.0). It employs a PCA technique applied to OMI radiances between 310.5 and 340 nm to derive principal spectral features from the full spectral content. The principal components (PCs) are used to represent various interfering processes in spectral fitting. This greatly reduces the OMI SO₂ spatially dependent biases as compared with the original OMI PBL product (Krotkov et al., 2006) and decreases retrieval noise by a factor of 2 (Li et al., 2013). Details of the PCA algorithm and the OMI PBL SO₂ data quality are provided in Li et al. (2013) and Krotkov et al. (2016). The product is publicly available from the NASA Goddard Earth Sciences (GES) Data and Information Services Center (DISC) (http://disc.sci.gsfc.nasa.gov/Aura/data-holdings/OMI/omso2_v003.shtml). It contains SO₂ vertical column densities (VCDs) in Dobson units (1 DU = 2.69 × 10¹⁶ molecules cm⁻²). Beginning in 2007, some OMI cross-track positions have been affected by FOV blockage and scattered light (i.e., the so-called the “row anomaly”) presumably caused by material associated with the satellite outside the instrument. We exclude pixels with nonzero values in the XTrackQualityFlag data field in the L1B data to avoid influence of the row anomaly. We also exclude pixels with large FOVs at the edges of the swath (rows < 5 or > 54, zero-based).

2.2 OMPS SO₂ data

The mapping component of the OMPS is a nadir-viewing UV spectrometer. The first model has been flying on board the NASA–NOAA Suomi National Polar-orbiting Partnership (SNPP) spacecraft since 2011 (Dittman et al., 2002; Flynn et al., 2014; Seftor et al., 2014). SNPP continues some of the long-term record of climate quality observations established by NASA's Earth Observation System (EOS) satel-

lites. It crosses the Equator each afternoon at about 13:30 LT, ~ 10 min ahead of the Aura Equator crossing time. OMPS measures backscattered UV radiance spectra from the Earth and solar irradiance in the 300–380 nm wavelength range at a spectral resolution of ~ 1 nm. It has a ~ 2800 km cross-track swath (110° FOV) with a nadir pixel size of $50 \text{ km} \times 50 \text{ km}$ in the nominal observation mode. Although it has coarser spectral and spatial resolutions and expected higher detection thresholds for emissions from point sources as compared with OMI (Fioletov et al., 2013), it is still suitable for monitoring large anthropogenic SO₂ pollution sources (Yang et al., 2013; Krotkov et al., 2016).

Here, we apply the same PCA retrieval technique described above to OMPS in order to obtain the total PBL SO₂ VCDs. The main difference between the OMPS and OMI PCA algorithms is that for the current OMI operational product, we only retrieve SO₂ for pixels with slant column ozone (O₃) < 1500 DU, while for OMPS we retrieve SO₂ for all pixels with solar zenith angle (SZA) $< 75^\circ$ in order to obtain better spatial coverage at high latitudes in winter (particularly near the edge of the swath). We have tested OMI retrievals using the same SZA threshold as OMPS and found results to be very similar to the operational product. Similar to the processing of OMI data, we also exclude OMPS pixels with large FOVs at the edges of the swath (rows < 2 or > 33 zero-based).

Another difference is that in the spectral fitting for the operational OMI product, up to 20 PCs derived from radiance data are used. For OMPS, we use up to 15 PCs. We found that fewer PCs are required in OMPS retrievals to achieve a background bias reduction similar to that for OMI. Both OMI and OMPS algorithms employ a simplified fixed SO₂ Jacobian table, calculated assuming the same surface albedo (0.05), surface pressure (1013.25 hPa), fixed SZA (30°), nadir-viewing zenith angle (0°), and O₃ and temperature profiles representative of typical midlatitude conditions (Krotkov et al., 2008). In the future, we plan to enhance the lookup table for SO₂ Jacobians to more accurately account for different measurement conditions.

2.3 OMI and OMPS data filtering and gridding

In order to account for different FOV sizes, we average both OMI and OMPS SO₂ pixels (level 2) to the same 0.5° latitude by 0.5° longitude grid daily from 2012 to 2015. Only mostly clear sky data, defined as pixels with effective cloud radiance fraction $< 30\%$, are used. The effective cloud radiance fraction is defined at each pixel as the fraction of the measured radiance that is scattered by clouds. The values are calculated and reported in the OMI and OMPS total ozone product. We also exclude large negative outliers in the data gridding (< -1 DU for OMI and < -0.5 DU for OMPS). The use of different thresholds accounts for the fact that the standard deviation of OMI retrievals over the presumably SO₂-free equatorial Pacific (~ 0.5 DU) is greater than that of OMPS

(~ 0.2 – 0.3 DU). The small systematic differences between retrievals from the two satellite instruments are mainly due to differences in how the simplified air mass factors (AMFs) relate to the true AMFs. In this paper, no empirical bias corrections are applied to the gridded SO₂ data. We plan to explore the use of empirical corrections to further improve the retrievals in the future.

2.4 Emission from OMI and OMPS

Emissions in this paper are estimated statistically using a “bottom-up” approach by fitting a parametric model to the average oversampled satellite SO₂ spatial patterns in the vicinity of each point source using a reference frame aligned with wind direction (Fioletov et al., 2015). Here, u and v wind components from European Centre for Medium-Range Weather Forecasts (ECMWF) reanalysis data (http://data-portal.ecmwf.int/data/d/interim_full_daily) are matched to each OMI FOV. All OMI data are rotated about the known source location in order to align with their wind vectors. This allows all OMI observations over a given period (1 year in this case) to be analyzed together in order to derive emissions by following the downwind decay of SO₂ plumes. These rotated OMI data along with wind speed are then fit to a three-parameter plume-like function that describes the crosswind distribution using a Gaussian and the downwind distribution using an exponentially modified Gaussian. A decay constant, representing an effective lifetime, and width parameter are specified, rather than fit, in order to improve the stability of the fitting (Fioletov et al., 2016). Values for these were derived by considering dozens of well-behaved SO₂ sources and found to exhibit a variability of less than 50%. Uncertainties of estimated annual emissions from individual sources are about 50%. However, comparisons with emissions measured directly at power plants stacks in the eastern US indicate better agreement ($\sim 20\%$). Local AMF corrections are applied to the OMI SO₂ data in the vicinity of each emission source as outlined in McLinden et al. (2016b). The OMI emissions used in the comparison below are taken directly from the global OMI SO₂ emission catalogue (Fioletov et al., 2016). OMPS emissions are calculated using a similar approach.

3 OMI and OMPS SO₂ spatial and temporal comparison

In this section, we compute two types of correlations. The first is the correlation between OMI and OMPS annual averaged SO₂ loading, which is computed for each pixel within a region. We refer to this as the OMI–OMPS “spatial correlation”. We also compute the correlation between daily OMI and OMPS SO₂ masses in specific regions over an extended time period; we refer to this as the OMI–OMPS “temporal correlation”.

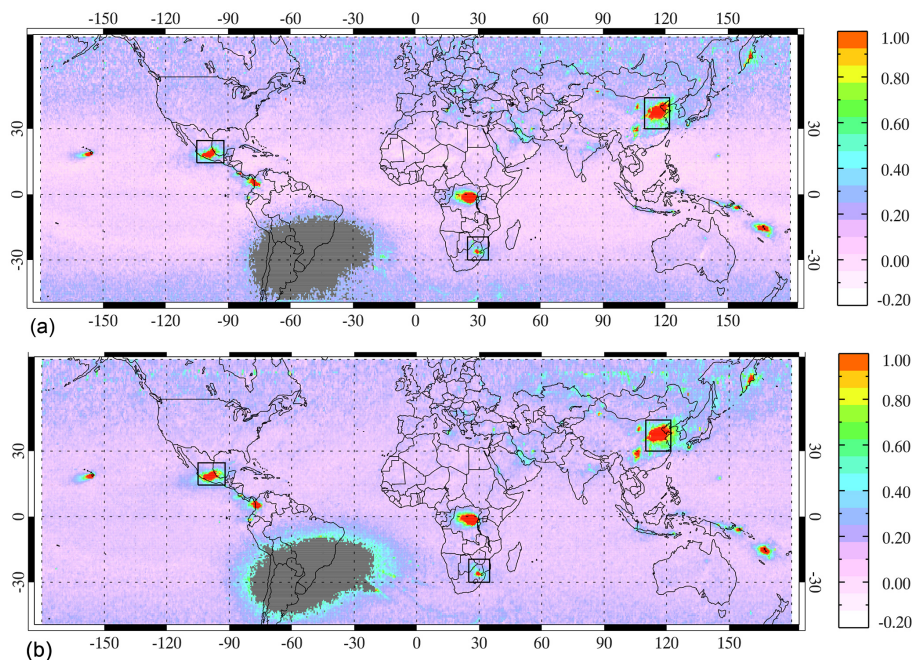


Figure 1. Annual SO₂ loading (unit: DU) in 2012 for OMI (a) and OMPS (b). Both OMI and OMPS SO₂ maps are gridded to $0.5^\circ \times 0.5^\circ$ grid cells. The three black boxes are regions for eastern China, Mexico, and South Africa, respectively, that will be examined in more detail below. The grey shaded area shows the area affected by the South Atlantic Anomaly.

3.1 Annual/regional average SO₂

In Fig. 1, we show that global annual average (2012) SO₂ columns from OMPS and OMI are generally consistent. Both OMI and OMPS PCA SO₂ data show regions with major anthropogenic pollution sources including eastern China, South Africa, Mexico, the Persian Gulf, and India, as well as a number of degassing and eruptive volcanoes (e.g., Mount Etna). For the regional comparisons, we focus on eastern China, Mexico, and South Africa. These are the regions affected by anthropogenic SO₂ pollution due to extensive emissions from coal-fired power plants and industrial processes (Krotkov et al., 2016). Mexico also has substantial volcanic SO₂ emissions from Popocatepetl volcano south of Mexico City (de Foy et al., 2009). The regions are situated in different latitude bands/climate zones and have different SO₂ loadings. This allows us to evaluate OMI and OMPS retrieval performance under a broad range of conditions. The three regions are outlined as black boxes in Fig. 1, and the coordinates are provided in Table 1. In the South Atlantic Anomaly (SAA) region, SO₂ data are screened by removing SO₂ columns greater than 0.3 DU. In this region, Earth's magnetic field traps high-energy charged particles. These particles can cause higher-than-normal irradiance to a low-Earth-orbiting satellite detector (e.g., OMI) and decrease the quality of measurements, notably in the UV.

Figure 2 shows that both OMPS and OMI capture the details of the annual average spatial distribution of the SO₂ pollution over the three regions examined in 2012. The av-

Table 1. The coordinates of each region.

	Latitude	Longitude
Eastern China	30° N, 42° N	110° E, 122° E
Mexico	14° N, 25° N	105° W, 92° W
South Africa	30° S, 20° S	25° E, 35° E

erage SO₂ pollution total columns over eastern China and Mexico are higher than over South Africa. The OMPS data show slightly higher SO₂ loading over eastern China and lower SO₂ loading over Mexico and South Africa as compared with OMI products. The annual regional averaged SO₂ columns over eastern China are 0.79 and 0.69 DU for OMPS and OMI, respectively. On an annual basis the OMI–OMPS spatial correlations are high. They are 0.96, 0.94, and 0.95 for eastern China, Mexico, and South Africa, respectively. Particularly over Mexico, the spatial patterns of high SO₂ (> 1 DU) from OMPS and OMI are similar. Regional annual average SO₂ loadings are 0.58 and 0.51 DU for OMPS and OMI, respectively, and the spatial correlation coefficient is 0.94. South Africa shows the smallest SO₂ loading and the best overall agreement between OMI and OMPS as compared with the other two regions. The regional annual average SO₂ loading from OMPS is 0.29 DU and from OMI is 0.28 DU. The spatial correlation coefficient for SO₂ loading between the two instruments in this region is 0.95. Three distinct “hot” spots (SO₂ loading > 0.53 DU) are captured by

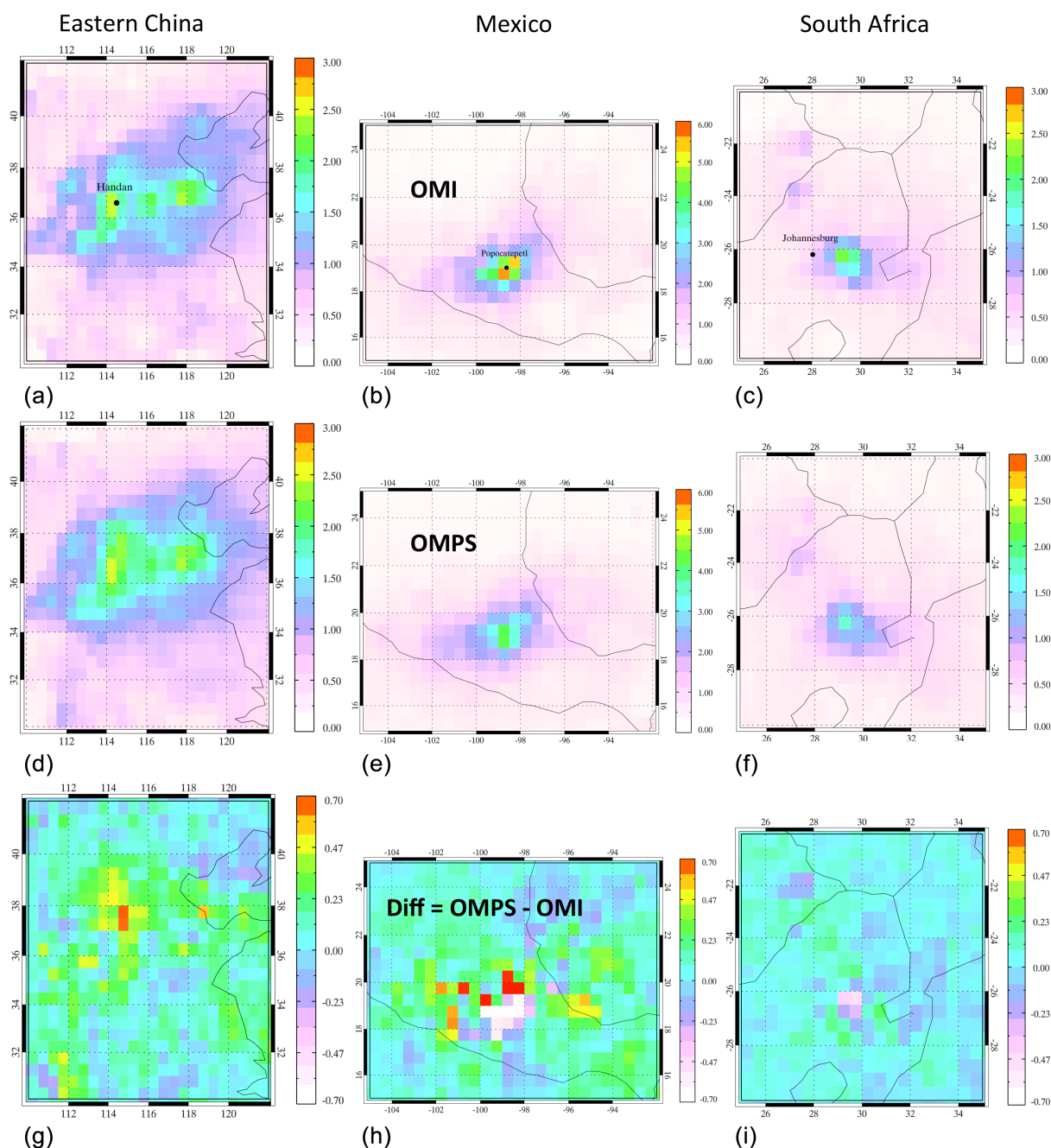


Figure 2. Annual SO₂ loading (unit: DU) over eastern China (left), Mexico (middle), and South Africa (right) for OMI (top), OMPS (center), and differences between OMPS and OMI (bottom, Diff = OMPS–OMI) in 2012. SO₂ columns amounts are gridded to 0.5° × 0.5° grid cells.

both OMPS and OMI in South Africa. These correspond to clusters of coal-fired power plants also detected in OMI NO₂ data (Duncan et al., 2016). We find that peak SO₂ columns from OMPS are smaller than from OMI, possibly due to the lower OMPS spatial resolution. This is less of an issue for eastern China, where the regional loading of SO₂ pollution is much higher and more homogeneous due to the numerous sources.

The differences in the spatial distributions of annual mean SO₂ between OMPS and OMI over these regions in 2012 are also presented in Fig. 2. Larger differences between the two instruments are found in areas with the strongest SO₂ sources. The maximum SO₂ differences between OMPS and OMI are 0.64 DU (29 %), –2.0 DU (–61 %), and –0.54 DU (–41 %) over eastern China, Mexico, and South Africa, respectively. For eastern China, the SO₂ loading is relatively

Table 2. The averaged SO₂ loading (unit: DU) in 2012–2015 from OMI and OMPS and their spatial correlations, r , for three regions: eastern China, Mexico, and South Africa.

	Eastern China				Mexico				South Africa			
	2012	2013	2014	2015	2012	2013	2014	2015	2012	2013	2014	2015
OMI	0.69	0.61	0.50	0.37	0.51	0.42	0.32	0.42	0.28	0.28	0.27	0.38
OMPS	0.79	0.67	0.52	0.36	0.58	0.45	0.34	0.41	0.29	0.29	0.28	0.35
r	0.96	0.96	0.95	0.92	0.94	0.97	0.95	0.94	0.95	0.96	0.97	0.95

high for the entire region due to the large cluster of point and area sources. The higher loading in OMPS retrievals may be due to the minor differences in algorithm implementation (see Sect. 2.2) and the different sampling between the two instruments. As for Mexico and South Africa, the SO₂ sources (and distributions) are more local. The negative bias of OMPS as compared with OMI may reflect the effect of different spatial resolutions between the two instruments and their capabilities of resolving point sources. In addition, the retrievals over Mexico are strongly affected by emissions from the Popocatepetl volcano (elevation 5426 m above sea level) and likely biased high since the volcanic plume is elevated while our retrievals assume a boundary layer profile. The elevated volcanic plume may be transported relatively quickly and the difference in sampling time between OMI and OMPS may cause relatively large differences in the spatial distributions. As a result, the difference between the two instruments may be exacerbated by the retrieval assumption of a boundary layer profile. The OMPS pixel size is about the same size as the 0.5° grid boxes used for comparisons. Emissions from a point SO₂ source could therefore alias into nearby grid boxes when we grid OMPS pixels. This may produce differences in gridded SO₂ data between OMPS and OMI. The difference is the largest for 2012, when Popocatepetl was most active with approximately 2 times the emissions of 2013 and 2014 (Fioletov et al., 2016). For these 2 latter years, the OMPS–OMI maximum differences are −0.69 and −0.68 DU, respectively.

Table 2 presents annual average SO₂ loading for each region and the OMI–OMPS spatial correlation for each year between 2012 and 2015. Over eastern China, the average SO₂ loading decreased significantly in 2015 as compared with 2012 (from ~0.69 DU in 2012 to ~0.37 DU in 2015 for OMI), in agreement with Krotkov et al. (2016). We note that the OMI–OMPS spatial correlation also decreases with reductions in the average SO₂ loading, possibly due to reductions in the SO₂ variability and thus a decrease in signal as compared with the noise.

3.2 Regional daily SO₂

In this section we compare regional SO₂ masses on a daily basis derived from the two instruments. Daily regional SO₂ masses are calculated as a sum of the SO₂ masses from the

grid cells (0.5° × 0.5°) that satisfy our filtering criteria (see Sect. 2.3). We only consider grid cells that have valid SO₂ retrievals from both instruments. This ensures consistent spatial sampling between the two instruments. We consider days only with the number of nonempty grid cells > 25 % of total grids cells in each region for both OMI and OMPS. Temporal correlations (r) between OMI and OMPS in Table 3 are calculated based on daily SO₂ masses from the two instruments that satisfy the above criteria. In Table 3, we show results of linear regression analyses using reduced major axis fitting that accounts for the uncertainties in both OMI and OMPS data. Results of the ordinary least-squares linear regression analyses are also provided in Table 3.

Figure 3 compares OMPS and OMI daily regional SO₂ masses over the eastern China domain from 2012 to 2015. The year 2013 has the best sampling (more than 200 days) and the best temporal correlation and slope between the instruments ($r = 0.88$ and the regression slope is 0.98). The other 3 years, despite reduced sampling, also have good temporal correlations ($r = 0.79$ – 0.85) and linear regression slopes close to unity (0.86 to 0.98). Although the SO₂ columns over the region remain the world's highest, the decreasing trend is also significant. Annual averaged OMI SO₂ masses in this region were 8.4, 8.8, 6.2, and 4.1 kt (kiloton, 10³ metric ton) (Table 5) in 2012, 2013, 2014, and 2015, respectively. This is in line with a ~50 % decrease over the North China Plain region also derived from OMI (Krotkov et al., 2016). Overall, OMPS SO₂ masses are slightly higher as compared with OMI. The temporal correlation between OMI and OMPS reduces from $r = 0.85$ – 0.88 in 2012–2013 to $r \sim 0.79$ in 2014–2015. The correlation decreases can be explained by reduced SO₂ emissions and pollution levels that bring SO₂ columns close to the OMI–OMPS detection limit and therefore scatter around a remaining offset. The eastern China area is located in the midlatitudes. High values of column O₃ in cold season are a major interfering species in SO₂ retrievals. This, together with higher solar zenith angles and possible snow events, leads to relatively large noise and potential biases in retrieved SO₂ in winter months. When we restrict our analysis to the warm season (April–October), the temporal correlation and regression slope between the two instruments improves especially for 2014 and 2015 ($r = 0.82$ – 0.87 and slope is 0.92–1.01; see Table 4).

Table 3. The total number of days with valid SO₂ for both OMI and OMPS for each year. Number of samples within ±50 and ±25 % agreement and percentage of the total sample, temporal correlation coefficient (*r*), and the slopes and intercepts from reduced major axis fitting and ordinary least-squares fitting for each year and all years. *X* represents OMI SO₂ and *Y* represents OMPS SO₂.

		Eastern China	Mexico	South Africa
2012	Total days:	143	141	163
	Reduced major axis:	$Y = 0.97X + 0.75$	$Y = 0.99X + 0.41$	$Y = 0.96X + 0.32$
	Ordinary least squares:	$Y = 0.83X + 2.56$	$Y = 0.95X + 0.72$	$Y = 0.86X + 0.78$
	Days within ±50 %:	129 (90 %)	121 (86 %)	145 (89 %)
	Days within ±25 %:	75 (52 %)	88 (62 %)	96 (59 %)
	<i>r</i> :	0.85	0.96	0.90
2013	Total days:	213	144	193
	Reduced major axis:	$Y = 0.98X + 0.93$	$Y = 0.99X + 0.86$	$Y = 0.96X + 0.25$
	Ordinary least squares:	$Y = 0.86X + 2.27$	$Y = 0.94X + 1.18$	$Y = 0.81X + 0.93$
	Days within ±50 %:	189 (89 %)	120 (83 %)	168 (87 %)
	Days within ±25 %:	109 (51 %)	79 (55 %)	108 (56 %)
	<i>r</i> :	0.88	0.96	0.84
2014	Total days:	159	133	186
	Reduced major axis:	$Y = 0.86X + 1.40$	$Y = 0.91X + 0.65$	$Y = 0.89X + 0.28$
	Ordinary least squares:	$Y = 0.68X + 3.00$	$Y = 0.83X + 1.05$	$Y = 0.78X + 0.77$
	Days within ±50 %:	134 (84 %)	109 (82 %)	164 (88 %)
	Days within ±25 %:	71 (45 %)	66 (50 %)	101 (54 %)
	<i>r</i> :	0.79	0.91	0.88
2015	Total days:	142	126	199
	Reduced major axis:	$Y = 0.91X + 0.41$	$Y = 0.95X + 0.68$	$Y = 0.76X + 0.93$
	Ordinary least squares:	$Y = 0.72X + 1.64$	$Y = 0.89X + 1.05$	$Y = 0.71X + 1.22$
	Days within ±50 %:	120 (85 %)	106 (84 %)	181 (91 %)
	Days within ±25 %:	78 (55 %)	75 (60 %)	116 (58 %)
	<i>r</i> :	0.79	0.94	0.94
2012–2015	Total days:	657	544	741
	Reduced major axis:	$Y = 0.96X + 0.68$	$Y = 0.97X + 0.60$	$Y = 0.80X + 0.82$
	Ordinary least squares:	$Y = 0.82X + 2.04$	$Y = 0.92X + 0.93$	$Y = 0.73X + 1.16$
	Days within ±50 %:	572 (87 %)	456 (84 %)	658 (89 %)
	Days within ±25 %:	333 (51 %)	308 (57 %)	421 (57 %)
	<i>r</i> :	0.86	0.95	0.91

The Mexico region is located in the tropics where the SO₂ retrievals from the PCA algorithm are less influenced by weather patterns and the total O₃ columns are less variable as compared with middle- and high-latitude regions. Due to the high frequency of cloud occurrence in this region, the number of days with valid SO₂ retrievals for each year is less than that from eastern China. Figure 4 shows that OMI and OMPS retrieved consistent SO₂ masses in all 4 years. The temporal correlation between the instruments is also the highest ($r = 0.91$ – 0.96) and regression line slopes are 0.91 – 0.99 ; i.e., this indicates that OMPS shows a relatively small multiplicative low bias as compared with OMI. As mentioned above, the SO₂ loading in Mexico region is subject to Popocatepetl eruptions. The increased sensitivity of the satellite instruments to SO₂ at higher altitudes possibly contributes to the OMI–OMPS SO₂ agreement over the Mexico region.

Compared with eastern China and Mexico, averaged SO₂ masses in South Africa are much smaller. The maximum SO₂ mass is less than 20 kt in 2012–2014 as shown in Fig. 5. The SO₂ mass exceeding 30 kt in April–May 2015 resulted from the passage of a volcanic SO₂ plume from the April 2015 Calbuco eruption in Chile (http://so2.gsfc.nasa.gov/pix/special/2015/calbuco/Calbuco_20150427_omiimps_1.html). After removing those days (total of 3 days), the linear regression slope increases from 0.76 to 0.83. The 2015 averaged SO₂ mass in the South Africa region decreases from 4.6 to 3.6 kt for OMPS and from 4.3 to 3.4 kt for OMI (see Table 5). Overall, SO₂ masses in the South Africa region from the two instruments are in good agreement.

We also investigated the correlation between the spatial distributions of the OMI and OMPS PCA retrievals on a daily basis as shown in Fig. 6. We excluded SO₂ masses < 2.5 kt

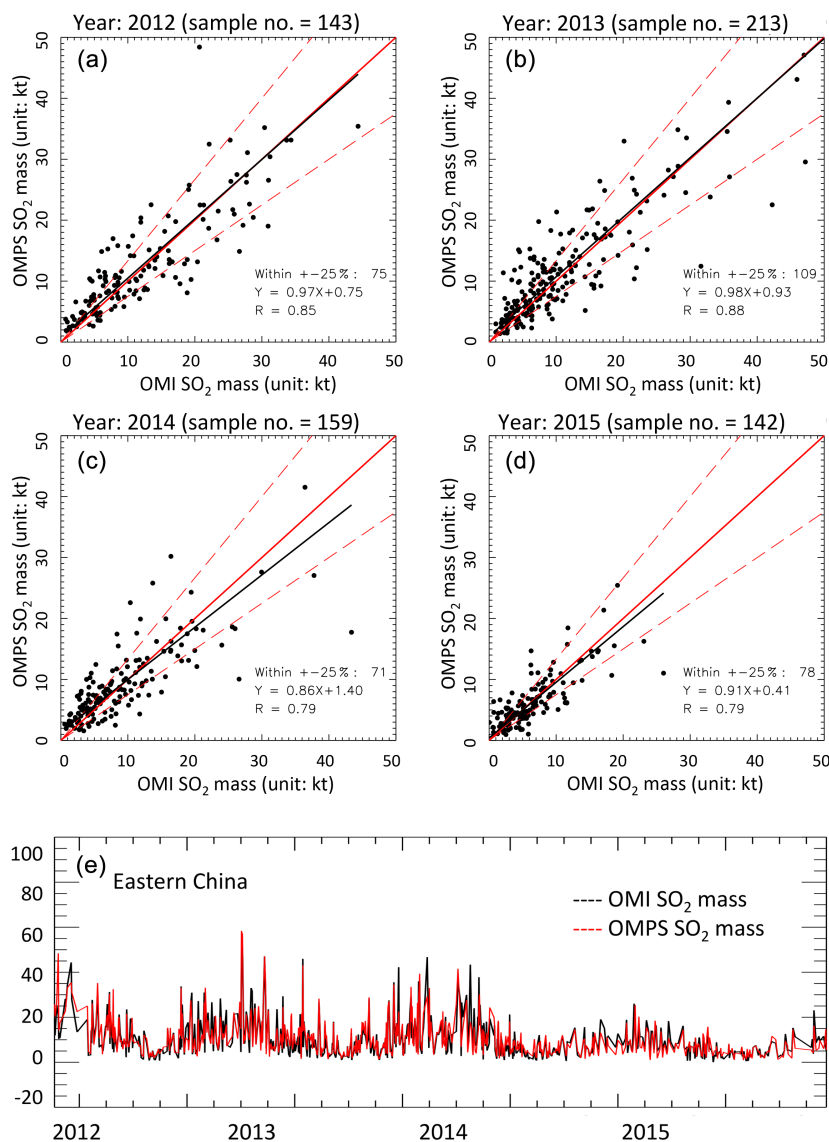


Figure 3. (a–d) Eastern China regional daily SO₂ mass (unit: kt) for OMI and OMPS for the years 2012, 2013, 2014, and 2015. Red solid line is the 1 : 1 line and dashed lines are $\pm 25\%$. Black line is the reduced major axis fitting of OMI and OMPS SO₂ masses. r is the temporal correlation coefficient. The number of samples within $\pm 25\%$ is also presented here. (e) Time series of daily SO₂ mass in the eastern China region from 2012 to 2015 with valid data for both OMI and OMPS.

over the area since, for those unpolluted days, OMI and OMPS retrievals are near their noise levels. Mexico shows the best correlation among the three regions; 82 % of the days have spatial correlation coefficient $r > 0.6$. The other two regions also have more than half of all qualified days with daily spatial correlation coefficients $r > 0.6$. These comparisons over the three regions suggest that the daily spatial distributions of SO₂ from OMI and OMPS PCA retrievals are correlated for even moderately polluted days. All three regions show that less than $\sim 50\%$ of the days have spatial correlation coefficient $r > 0.7$. The discrepancy between the two instruments is probably a result of different spatial

resolutions. OMPS large pixels can effectively cause SO₂ to spill out into the adjacent areas when averaging over our grid boxes. Li et al. (2017) used a volcanic case to demonstrate how the OMPS low spatial resolution produced lower SO₂ columns as compared with OMI (Li et al., 2017, their Fig. S8).

3.3 Instrument performance and trends

Instrument degradation may affect SO₂ retrievals. We examined the trends in spatial standard deviation (SD) and standard errors (SE = SD divided by the square root of the number of daily observations) of the daily SO₂ noise over three

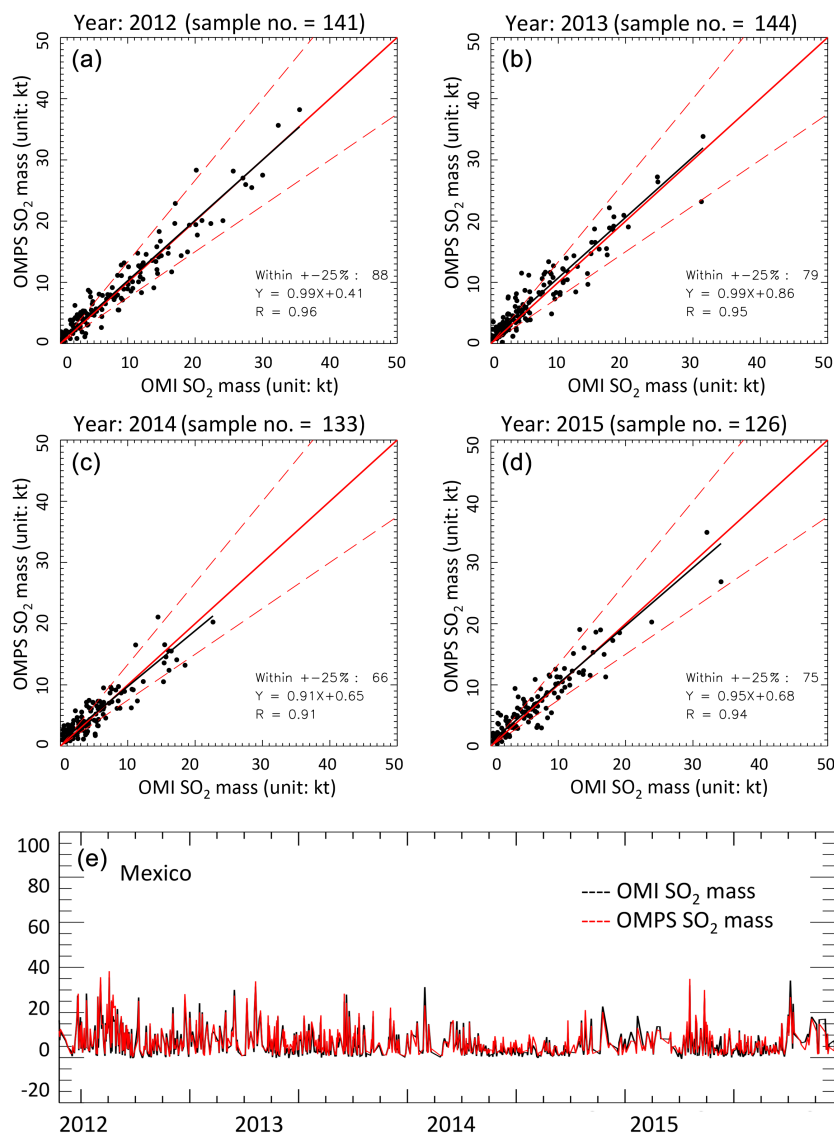


Figure 4. Same as Fig. 3 but for the Mexico region.

clean regions in the Pacific (150–120° W). Figure 7 shows the median and 25th and 75th percentiles of daily SO₂ SD and SE in August in each year. In addition to the tropical Pacific region between 10° S and 10° N, we selected the same latitudes as those of our eastern China and South Africa regions (called north and south Pacific regions, respectively) and similar filtering has been applied to the data. Over these background regions, the SO₂ levels are below satellite detection limits and, as expected, the medians of daily averaged SO₂ columns were statistically equal to zero for the regions (−0.06–0.04 DU for OMI and 0.07–0.1 DU for OMPS). The OMI SDs increased by $\sim 10\%$ from 2005 to 2015 over the north Pacific and tropical Pacific regions, which can be explained by increased CCD detector noise after 12 years of continuous operation in space. As expected the OMPS SDs

do not show significant changes during its first 4 years in space. We note that OMPS SDs (~ 0.3 DU) are roughly half the OMI values ($\sim 0.5 = -0.7$ DU), which can be explained in part by the larger OMPS FOV that results in higher signal-to-noise ratio as well as OMI long-term degradation. OMPS large FOVs may also reduce errors generated by variability in observation conditions (by smoothing them out) that affect our simple fixed AMF assumptions, e.g., geometry, cloudiness, and surface conditions. We plan to re-examine this issue with future versions of the PCA algorithm that will have more detailed AMF calculations. OMI SEs in 2005 are actually smaller than OMPS in 2012, which may be explained by higher OMI spatial resolution and a resulting larger number of measurements over the same region. However, the OMI SEs increased after 2008 due to the row anomaly that

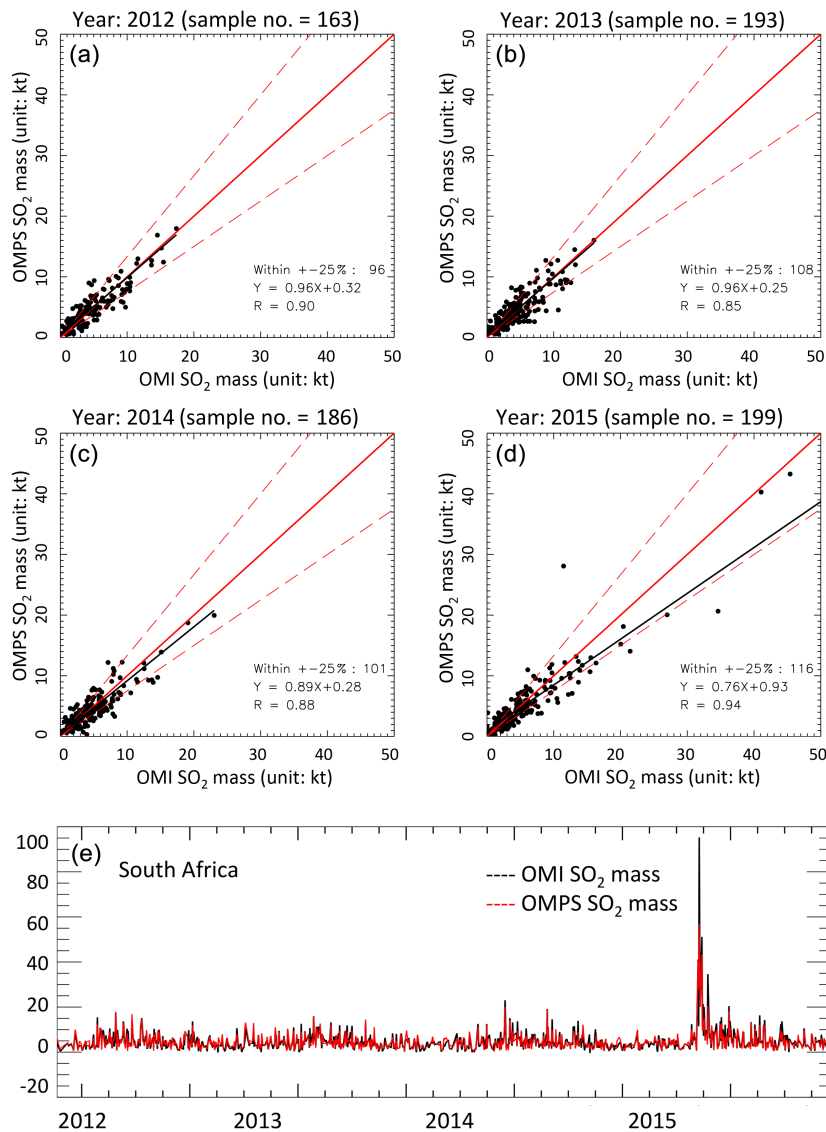


Figure 5. Same as Fig. 3 but for the South Africa region.

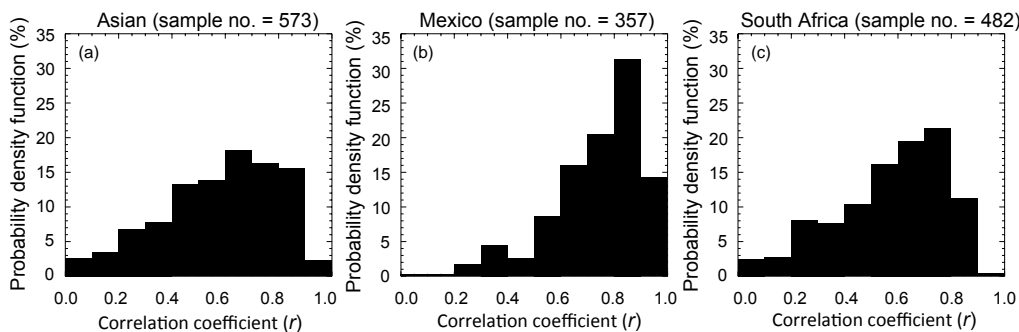


Figure 6. Probability distribution functions (PDFs) of daily spatial correlations over eastern China (a), Mexico (b), and South Africa (c) from 2012 to 2015.

Table 4. Same as Table 3 but for the warm season (April–October) over eastern China.

2012	Total days:	105
	Reduced major axis:	$Y = 0.92X + 1.00$
	Ordinary least squares:	$Y = 0.80X + 2.21$
	r :	0.87
2013	Total days:	132
	Reduced major axis:	$Y = 0.95X + 1.62$
	Ordinary least squares:	$Y = 0.83X + 2.67$
	r :	0.87
2014	Total days:	101
	Reduced major axis:	$Y = 0.98X + 1.12$
	Ordinary least squares:	$Y = 0.83X + 2.09$
	r :	0.85
2015	Total days:	96
	Reduced major axis:	$Y = 1.01X + 0.46$
	Ordinary least squares:	$Y = 0.83X + 1.34$
	r :	0.82

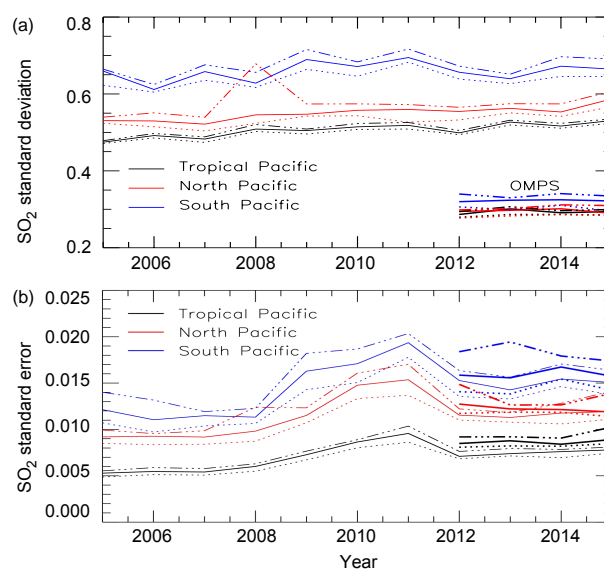
Table 5. Averaged SO₂ mass (unit: kt) over eastern China, Mexico, and South Africa in 2012, 2013, 2014, and 2015 for both OMI and OMPS.

		2012	2013	2014	2015
Eastern China	OMI	8.4	8.8	6.2	4.1
	OMPS	9.1	9.8	6.4	4.0
Mexico	OMI	5.9	4.2	3.2	4.0
	OMPS	6.3	4.9	3.4	4.4
South Africa	OMI	3.3	3.3	3.2	4.6
	OMPS	3.4	3.3	3.1	4.3

decreased the number of available observations. OMI and OMPS SEs became comparable in recent years. In other months, SDs and SEs show similar trends as those shown for August. But winter months (October–February) show more interannual variations compared to other months (see Supplement) because winter months are more likely influenced by pollution transport from other regions as compared with other months.

4 Emission comparison of SO₂ emissions estimated from OMI and OMPS PCA retrievals

In this section, we evaluate OMPS' ability to continue space-based monitoring of SO₂ emissions from large point sources. It has been recently demonstrated that, by combining wind data and OMI PCA PBL SO₂ retrievals, one can quantify emissions from more than 490 anthropogenic and volcanic sources around the globe (Fioletov et al., 2015, 2016). This top-down approach is independent of the conventional bottom-up method and has helped to uncover a number of

**Figure 7.** Standard deviation (SD, **a**) and standard error (SE, **b**) of SO₂ noise (DU) averaged over clean background regions in the Pacific (150–120° W), in the north between 30 and 42° N (Red), in the tropics between 10° S and 10° N (black), and in the south between 30 and 20° S (blue) in August of each year from 2005 to 2015. Solid lines are medians of daily SO₂ SD from each month (31 days), and dashed lines are 25 and 75 % of daily SO₂ SD from each month, respectively. OMI data start in 2005 and OMPS data start in 2012. The OMI SD peak in 2008 over north Pacific results from the Okmok and Kasatochi eruptions (Krotkov et al., 2010).

SO₂ sources that are missing or underreported in some leading emission inventories using OMI data (McLinden et al., 2016b). Here we apply the same method to OMPS SO₂ data to estimate emissions for the same point sources and compare the OMPS-based emission estimates with those from OMI. It should be noted that the OMPS-based results presented in this section are preliminary, as the emission derivation method has been developed and optimized for use with OMI. In particular, the method includes a step in which local bias is estimated and removed from satellite data. Since OMPS has a much larger footprint and far less pixels as compared with OMI, its local bias has to be estimated from a much larger domain. Nonetheless, the comparison in this section should offer some insights into the performance of SNPP OMPS in SO₂ emission monitoring.

Figure 8a shows the locations of ~400 large point sources and their average annual SO₂ emissions during 2012–2015 estimated from OMI retrievals. OMPS-based emission estimates for these sources (Fig. 8b) show a generally similar spatial distribution, with numerous large anthropogenic sources in China, India, and the Middle East, as well as a number of active degassing volcanoes around the Pacific Ocean. This similarity is not surprising given that the annual mean SO₂ loadings derived with the PCA algorithm is largely consistent between the two instruments (Fig. 1).

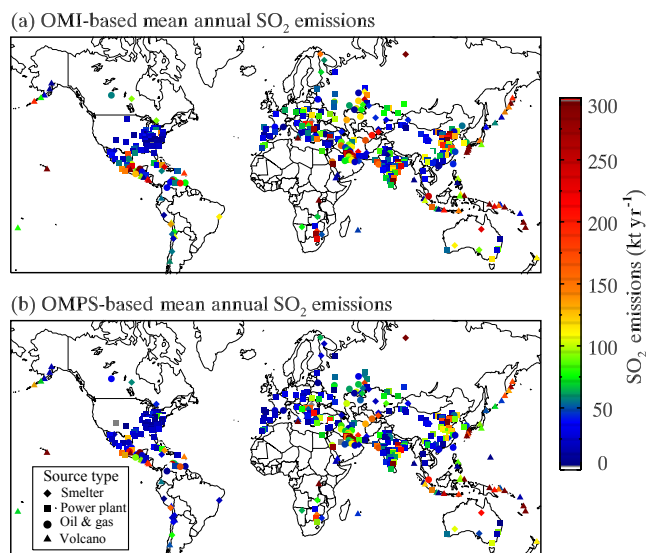


Figure 8. (a) Average annual SO₂ emissions during 2012–2015 estimated from the operational OMI PCA PBL SO₂ retrievals for 403 point sources worldwide. (b) Same as panel (a) but with emissions estimated from OMPS retrievals. Color represents the magnitude of the estimated emissions while source types are marked with different symbols.

However, one may notice that OMPS-based emission estimates tend to be smaller than OMI. A linear regression analysis (Fig. 9) indicates that for all 4 years in our study period, the emissions estimated using OMPS and OMI data are highly correlated, with correlation coefficient of 0.91–0.97. The slope ranges between 0.88 and 0.97, suggesting that OMPS underestimates emissions as compared with OMI. The OMI- and OMPS-based annual emissions agree to within $\pm 25\%$ of each other for about one third of the large 403 sources (i.e., 132–149 for different years). If we exclude volcanic sources from the regression analysis, the OMI and OMPS-based emission estimates for anthropogenic sources are still in relatively good agreement, with correlation coefficients of 0.93–0.94 and slopes of 0.85–0.98 for all years.

It has been shown that point sources emitting more than $\sim 30\text{--}40\text{ kt SO}_2$ each year can be detected from OMI PCA retrievals (Fioletov et al., 2015). Detection of smaller sources may be possible in some cases but is more uncertain. Indeed, if we require that, for a source to be considered as being detected, its estimated annual emissions must be greater than or equal to twice the associated emission uncertainty (estimated by the emission estimation algorithm), only ~ 20 of those sources detected by OMI in 2012 have emissions below 30 kt yr^{-1} (Fig. 10a). Based on this criterion, OMPS is only capable of detecting a fraction of these OMI-detected sources (Fig. 10a). This fraction increases with the strength of emissions (Fig. 10b). It is generally below 50 % for sources of $10\text{--}50\text{ kt yr}^{-1}$, but it grows to $\sim 60\text{--}80\%$ for sources of 60--

130 kt yr^{-1} . For even larger sources, this fraction is close to 100 %.

Overall, our comparison between SO₂ emissions derived from the two instruments suggests that OMI- and OMPS-based emissions are highly correlated and that OMPS-based emissions are slightly smaller, probably reflecting its reduced sensitivity to anthropogenic sources due to coarser spatial resolution. The OMPS detection limit for point sources is probably $\sim 80\text{--}100\text{ kt yr}^{-1}$, greater than the previously estimated OMI detection limit of $30\text{--}40\text{ kt yr}^{-1}$ (Fioletov et al., 2016). Despite these differences, OMPS is capable of detecting the majority of point sources detected by OMI as compared with only 30–40 sources that are detectable with GOME-2 and SCIAMACHY (Fioletov et al., 2013). This is due in part to the relatively low noise level of OMPS that partially compensates for its larger footprint; unlike OMI, OMPS does not have significantly more pixels in the fitting area as compared with GOME-2 or SCIAMACHY. However, the uncertainty in derived SO₂ emissions tends to be smaller for OMPS as compared with GOME-2 or SCIAMACHY. Global total anthropogenic emissions (for the 403 sources) are 24 Tg yr^{-1} from OMPS and 30 Tg yr^{-1} from OMI; bottom-up inventories indicate total anthropogenic emissions of $100\text{--}110\text{ Tg yr}^{-1}$, albeit for an earlier period (Janssens-Maenhout et al., 2015; Klimont et al., 2013). This suggests OMPS is able to detect roughly 25 % of the total anthropogenic source.

5 Conclusions

Taking advantage of the 4-year overlap between OMI and OMPS local afternoon measurements and applying the same PCA algorithm to retrieve SO₂, we demonstrate that OMI and OMPS SO₂ retrievals are highly consistent for the world's most polluted regions from 2012 through 2015. The annually averaged OMI–OMPS spatial correlation coefficients of SO₂ loading over eastern China, Mexico, and South Africa are greater than ~ 0.9 in each year. The daily regional SO₂ temporal correlation coefficients are 0.86, 0.95, and 0.91 for eastern China, Mexico, and South Africa, respectively. The difference of regional averaged SO₂ mass is less than 10 % between the two instruments for the three regions in each year except over Mexico in 2013, when the difference is 14 %. The comparison of ~ 400 global anthropogenic and volcanic SO₂ emissions, derived from OMI and OMPS retrievals using a top-down approach, indicates that the correlations between OMI and OMPS annual emissions are high ($r \gtrsim 0.9$). OMPS is capable of detecting sources about 50 % of sources with emissions of $10\text{--}50\text{ kt yr}^{-1}$ that are detected with OMI and close to 100 % of sources larger than 130 kt yr^{-1} detected with OMI. Good consistency between the two instruments provides confidence that the OMPS nadir mapper currently flying on board the SNPP satellite and similar future instruments planned for the follow-up JPSS 1, 2,

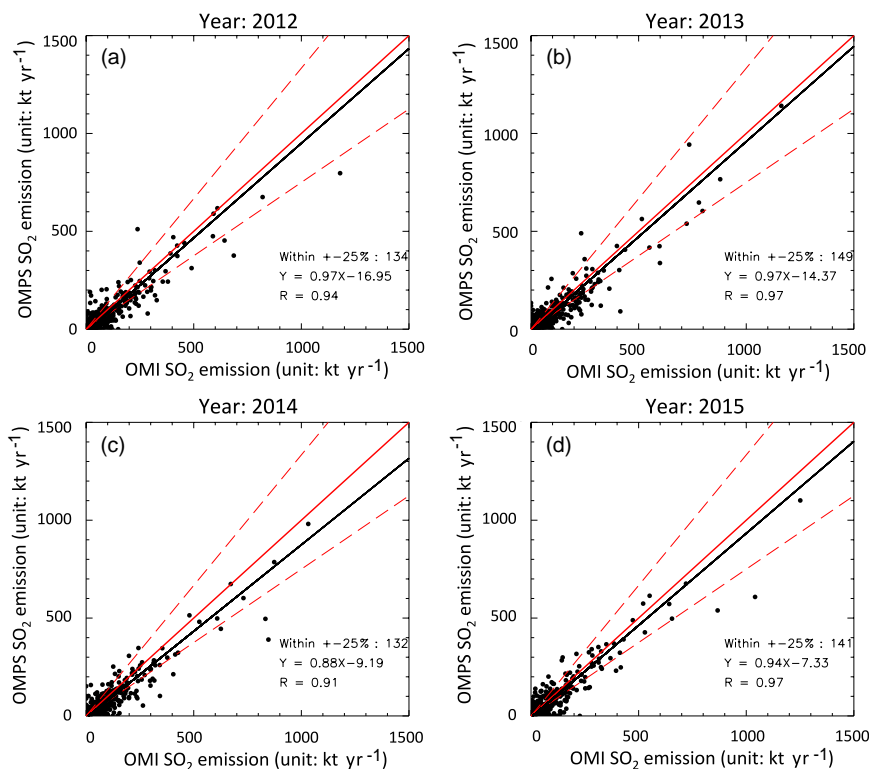


Figure 9. Scatterplots comparing the annual SO₂ emissions estimated using OMPS and OMI retrievals for 403 sources (see Fig. 8 for their locations) indicate generally good agreement between the two datasets, with correlation coefficients between 0.91 and 0.97 and slopes between 0.88 and 0.97.

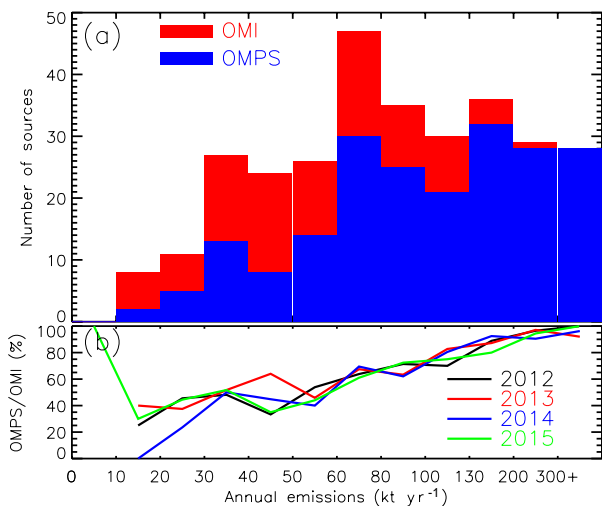


Figure 10. (a) Red (blue) bars: the number of SO₂ sources within different emission bins detected using OMI (OMPS) PCA retrievals for 2012. For a source to be counted as a successful detection, its estimated annual emissions have to be at least twice the associated uncertainty; (b) the percentage of OMI-detected sources within each bin that is also detected by OMPS in different years.

3, and 4 NOAA operational satellites with improved spatial resolution similar to OMI, can be used to continue long-term OMI SO₂ record started in 2004.

Data availability. The OMI PBL SO₂ product (OMSO2 v1.2.0) is publicly available from the NASA Goddard Earth Sciences (GES) Data and Information Services Center (DISC) (http://disc.sci.gsfc.nasa.gov/Aura/data-holdings/OMI/omso2_v003.shtml; NASA GES DISC, 2017).

The OMPS PBL monthly SO₂ product is publicly available from NASA/GSFC Aura Validation Data Center (AVDC) (<http://avdc.gsfc.nasa.gov/index.php?site=1868800100>; NASA/GSFC AVDC, 2017).

The Supplement related to this article is available online at [doi:10.5194/amt-10-1495-2017-supplement](https://doi.org/10.5194/amt-10-1495-2017-supplement).

Competing interests. The authors declare that they have no conflict of interest.

Acknowledgements. The authors acknowledge the NASA Earth Science Division (ESD) Aura Science Team program for funding of OMI product development and analysis. The Dutch- and Finnish-

built OMI instrument is part of the NASA's Earth Observing System (EOS) Aura satellite payload. The OMI project is managed by the Royal Meteorological Institute of the Netherlands (KNMI) and the Netherlands Space Agency (NSO). Can Li acknowledges partial support from NASA's Earth Science New Investigator program in developing the OMPS SO₂ algorithm (grant no. NNX14AI02G).

The authors would like to thank the NASA OMPS ozone Product Evaluation and Test Element (PEATE) team for updating the OMPS calibration and producing the OMPS Level 1b data used in this analysis. We thank the OMI calibration team, led by KNMI, for the calibrated OMI level 1b data used here and the Atmospheric Chemistry Processing System (ACPS) team for processing the OMI data.

Edited by: A. Richter

Reviewed by: three anonymous referees

References

- Carn, S. A., Krueger, A. J., Krotkov, N. A., Yang, K., and Levelt, P. F.: Sulfur dioxide emissions from Peruvian copper smelters detected by the Ozone Monitoring Instrument, *Geophys. Res. Lett.*, 34, L09801, doi:10.1029/2006GL029020, 2007.
- de Foy, B., Krotkov, N. A., Bei, N., Herndon, S. C., Huey, L. G., Martínez, A.-P., Ruiz-Suárez, L. G., Wood, E. C., Zavala, M., and Molina, L. T.: Hit from both sides: tracking industrial and volcanic plumes in Mexico City with surface measurements and OMI SO₂ retrievals during the MILAGRO field campaign, *Atmos. Chem. Phys.*, 9, 9599–9617, doi:10.5194/acp-9-9599-2009, 2009.
- Dittman, M. G., Ramberg, E., Chrisp, M., Rodriguez, J. V., Sparks, A. L., Zaun, N. H., Hendershot, P., Dixon, T., Philbrick, R. H., and Wasinger, D.: Nadir ultraviolet imaging spectrometer for the NPOESS Ozone Mapping and Profiler Suite (OMPS), *Proc. SPIE* 4814, Earth Observing Systems VII, 111–119, doi:10.1117/12.453748, 2002.
- Duncan, B. N., Lamsal, L. N., Thompson, A. M., Yoshida, Y., Lu, Z., Streets, D. G., Hurwitz, M. M., and Pickering, K. E.: A space-based, high-resolution view of notable changes in urban NO_x pollution around the world (2005–2014), *J. Geophys. Res.-Atmos.*, 121, 976–996, doi:10.1002/2015JD024121, 2016.
- Eisinger, M. and Burrows, J. P.: Tropospheric sulfur dioxide observed by the ERS-2 GOME instrument, *Geophys. Res. Lett.*, 25, 4177–4180, doi:10.1029/1998GL900128, 1998.
- Faloona, I., Conley, S. A., Blomquist, B., Clarke, A. D., Kapustin, V., Howell, S., Lenschow, D. H., and Bandy, A. R.: Sulfur dioxide in the tropical marine boundary layer: dry deposition and heterogeneous oxidation observed during the Pacific Atmospheric Sulfur Experiment, *J. Atmos. Chem.*, 63, 13–32, doi:10.1007/s10874-010-9155-0, 2010.
- Fioletov, V. E., McLinden, C. a., Krotkov, N., Yang, K., Loyola, D. G., Valks, P., Theys, N., Van Roozendaal, M., Nowlan, C. R., Chance, K., Liu, X., Lee, C., and Martin, R. V.: Application of OMI, SCIAMACHY, and GOME-2 satellite SO₂ retrievals for detection of large emission sources, *J. Geophys. Res.-Atmos.*, 118, 11399–11418, doi:10.1002/jgrd.50826, 2013.
- Fioletov, V. E., McLinden, C. A., Krotkov, N., and Li, C.: Lifetimes and emissions of SO₂ from point sources estimated from OMI, *Geophys. Res. Lett.*, 42, 1969–1976, doi:10.1002/2015GL063148, 2015.
- Fioletov, V. E., McLinden, C. A., Krotkov, N., Li, C., Joiner, J., Theys, N., Carn, S., and Moran, M. D.: A global catalogue of large SO₂ sources and emissions derived from the Ozone Monitoring Instrument, *Atmos. Chem. Phys.*, 16, 11497–11519, doi:10.5194/acp-16-11497-2016, 2016.
- Flynn, L., Long, C., Wu, X., Evans, R., Beck, C. T., Petropavlovskikh, I., McConville, G., Yu, W., Zhang, Z., Niu, J., Beach, E., Hao, Y., Pan, C., Sen, B., Novicki, M., Zhou, S., and Seftor, C.: Performance of the Ozone Mapping and Profiler Suite (OMPS) products, *J. Geophys. Res.-Atmos.*, 119, 6181–6195, doi:10.1002/2013JD020467, 2014.
- Janssens-Maenhout, G., Crippa, M., Guizzardi, D., Dentener, F., Muntean, M., Pouliot, G., Keating, T., Zhang, Q., Kurokawa, J., Wankmüller, R., Denier van der Gon, H., Kuenen, J. J. P., Klimont, Z., Frost, G., Darras, S., Koffi, B., and Li, M.: HTAP_v2.2: a mosaic of regional and global emission grid maps for 2008 and 2010 to study hemispheric transport of air pollution, *Atmos. Chem. Phys.*, 15, 11411–11432, doi:10.5194/acp-15-11411-2015, 2015.
- Klimont, Z., Smith, S. J., and Cofala, J.: The last decade of global anthropogenic sulfur dioxide: 2000–2011 emissions, *Environ. Res. Lett.*, 8, 014003, doi:10.1088/1748-9326/8/1/014003, 2013.
- Krotkov, N. A., Cam, S. A., Krueger, A. J., Bhartia, P. K., and Yang, K.: Band residual difference algorithm for retrieval of SO₂ from the Aura Ozone Monitoring Instrument (OMI), *IEEE Trans. Geosci. Remote Sens.*, 44, 1259–1266, doi:10.1109/TGRS.2005.861932, 2006.
- Krotkov, N. A., McClure, B., Dickerson, R. R., Carn, S. A., Li, C., Bhartia, P. K., Yang, K., Krueger, A. J., Li, Z., Levelt, P. F., Chen, H., Wang, P., and Lu, D.: Validation of SO₂ retrievals from the Ozone Monitoring Instrument over NE China, *J. Geophys. Res.-Atmos.*, 113, D16S40, doi:10.1029/2007JD008818, 2008.
- Krotkov, N. A., Schoeberl, M. R., Morris, G. A., Carn, S., and Yang, K.: Dispersion and lifetime of the SO₂ cloud from the August 2008 Kasatochi eruption, *J. Geophys. Res.*, 115, D00L20, doi:10.1029/2010JD013984, 2010.
- Krotkov, N. A., McLinden, C. A., Li, C., Lamsal, L. N., Celarier, E. A., Marchenko, S. V., Swartz, W. H., Bucseles, E. J., Joiner, J., Duncan, B. N., Boersma, K. F., Veeffkind, J. P., Levelt, P. F., Fioletov, V. E., Dickerson, R. R., He, H., Lu, Z., and Streets, D. G.: Aura OMI observations of regional SO₂ and NO₂ pollution changes from 2005 to 2015, *Atmos. Chem. Phys.*, 16, 4605–4629, doi:10.5194/acp-16-4605-2016, 2016.
- Krueger, A. J.: Sighting of El Chichon sulfur dioxide clouds with the Nimbus 7 total ozone mapping spectrometer, *Science*, 220, 1377–1379, doi:10.1126/science.220.4604.1377, 1983.
- Lee, C., Martin, R. V., Van Donkelaar, A., O'Byrne, G., Krotkov, N., Richter, A., Huey, L. G., and Holloway, J. S.: Retrieval of vertical columns of sulfur dioxide from SCIAMACHY and OMI: Air mass factor algorithm development, validation, and error analysis, *J. Geophys. Res.-Atmos.*, 114, D22303, doi:10.1029/2009JD012123, 2009.
- Levelt, P. F., Hilsenrath, E., Leppelmeier, G. W., Van Den Oord, G. H. J., Bhartia, P. K., Tamminen, J., De Haan, J. F., and Veeffkind, J. P.: Science Objectives of the Ozone Monitoring Instrument, *IEEE T. Geosci. Remote*, 44, 1199–1208, 2006a.

- Levelt, P. F., Van Den Oord, G. H. J., Dobber, M. R., Mälkki, A., Visser, H., De Vries, J., Stammes, P., Lundell, J. O. V., and Saari, H.: The Ozone Monitoring Instrument, *IEEE Trans. Geosci. Remote Sens.*, 44, 1093–1101, 2006b.
- Li, C., Zhang, Q., Krotkov, N. A., Streets, D. G., He, K., Tsay, S.-C., and Gleason, J. F.: Recent large reduction in sulfur dioxide emissions from Chinese power plants observed by the Ozone Monitoring Instrument, *Geophys. Res. Lett.*, 37, L08807, doi:10.1029/2010GL042594, 2010a.
- Li, C., Krotkov, N. A., Dickerson, R. R., Li, Z., Yang, K., and Chin, M.: Transport and evolution of a pollution plume from northern China: A satellite-based case study, *J. Geophys. Res.*, 115, D00K03, doi:10.1029/2009JD012245, 2010b.
- Li, C., Joiner, J., Krotkov, N. A., and Bhartia, P. K.: A fast and sensitive new satellite SO₂ retrieval algorithm based on principal component analysis: Application to the ozone monitoring instrument, *Geophys. Res. Lett.*, 40, 6314–6318, doi:10.1002/2013GL058134, 2013.
- Li, C., Krotkov, N. A., Carn, S., Zhang, Y., Spurr, R. J. D., and Joiner, J.: New-generation NASA Aura Ozone Monitoring Instrument (OMI) volcanic SO₂ dataset: algorithm description, initial results, and continuation with the Suomi-NPP Ozone Mapping and Profiler Suite (OMPS), *Atmos. Meas. Tech.*, 10, 445–458, doi:10.5194/amt-10-445-2017, 2017.
- McLinden, C. A., Fioletov, V., Boersma, K. F., Kharol, S. K., Krotkov, N., Lamsal, L., Makar, P. A., Martin, R. V., Veefkind, J. P., and Yang, K.: Improved satellite retrievals of NO₂ and SO₂ over the Canadian oil sands and comparisons with surface measurements, *Atmos. Chem. Phys.*, 14, 3637–3656, doi:10.5194/acp-14-3637-2014, 2014.
- McLinden, C. A., Fioletov, V., Krotkov, N. A., Li, C., Boersma, K. F., and Adams, C.: A Decade of Change in NO₂ and SO₂ over the Canadian Oil Sands As Seen from Space, *Environ. Sci. Technol.*, 50, 331–337, doi:10.1021/acs.est.5b04985, 2016a.
- McLinden, C. A., Fioletov, V., Shephard, M. W., Krotkov, N., Li, C., Martin, R. V., Moran, M. D., and Joiner, J.: Space-based detection of missing sulfur dioxide sources of global air pollution, *Nat. Geosci.*, 9, 496–500, doi:10.1038/ngeo2724, 2016b.
- NASA Goddard Earth Sciences (GES) Data and Information Services Center (DISC): The OMI PBL SO₂ product (OMSO2v1.2.0), available at: http://disc.sci.gsfc.nasa.gov/Aura/data-holdings/OMI/omso2_v003.shtml, last access: 18 April 2017.
- NASA/GSFC Aura Validation Data Center (AVDC): The OMPS PBL monthly SO₂, available at: <http://avdc.gsfc.nasa.gov/index.php?site=1868800100>, last access: 18 April 2017.
- Nowlan, C. R., Liu, X., Chance, K., Cai, Z., Kurosu, T. P., Lee, C., and Martin, R. V.: Retrievals of sulfur dioxide from the Global Ozone Monitoring Experiment 2 (GOME-2) using an optimal estimation approach: Algorithm and initial validation, *J. Geophys. Res.*, 116, D18301, doi:10.1029/2011JD015808, 2011.
- Schoeberl, M. R., Douglass, A. R., Hilsenrath, E., Bhartia, P. K., Beer, R., Waters, J. W., Gunson, M. R., Froidevaux, L., Gille, J. C., Barnett, J. J., Levelt, P. F., and DeCola, P.: Overview of the EOS aura mission, *IEEE Trans. Geosci. Remote Sens.*, 44, 1066–1072, doi:10.1109/TGRS.2005.861950, 2006.
- Seftor, C. J., Jaross, G., Kowitz, M., Haken, M., Li, J., and Flynn, L. E.: Postlaunch performance of the Suomi National Polar-orbiting Partnership Ozone Mapping and Profiler Suite (OMPS) nadir sensors, *J. Geophys. Res.-Atmos.*, 119, 4413–4428, doi:10.1002/2013JD020472, 2014.
- Smith, S. J., van Aardenne, J., Klimont, Z., Andres, R. J., Volke, A., and Delgado Arias, S.: Anthropogenic sulfur dioxide emissions: 1850–2005, *Atmos. Chem. Phys.*, 11, 1101–1116, doi:10.5194/acp-11-1101-2011, 2011.
- Theys, N., De Smedt, I., van Gent, J., Danckaert, T., Wang, T., Hendrick, F., Stavrou, T., Bauduin, S., Clarisse, L., Li, C., Krotkov, N., Yu, H., Brenot, H., and Van Roozendael, M.: Sulfur dioxide vertical column DOAS retrievals from the Ozone Monitoring Instrument: Global observations and comparison to ground-based and satellite data, *J. Geophys. Res.-Atmos.*, 120, 2470–2491, doi:10.1002/2014JD022657, 2015.
- Yang, K., Dickerson, R. R., Carn, S. A., Ge, C., and Wang, J.: First observations of SO₂ from the satellite Suomi NPP OMPS: Widespread air pollution events over China, *Geophys. Res. Lett.*, 40, 4957–4962, doi:10.1002/grl.50952, 2013.